2011

Global upper ocean heat content and climate variability

Chu, Peter C.

Chu, P.C., 2011: Global upper ocean heat content and climate variability. Ocean Dynamics, 61 (8), 1189-1204 (paper download).
http://hdl.handle.net/10945/36116

Ocean Dynamics (2011) 61:1189–1204
DOI 10.1007/s10236-011-0411-x

Global upper ocean heat content and climate variability

Peter C. Chu

Received: 25 August 2010 / Accepted: 15 March 2011 / Published online: 11 May 2011

Abstract Observational data from the Global Temperature and Salinity Profile Program were used to calculate the upper ocean heat content (OHC) anomaly. The thickness of the upper layer is taken as 300 m for the Pacific/Atlantic Ocean and 150 m for the Indian Ocean since the Indian Ocean has shallower thermoclines. First, the optimal spectral decomposition scheme was used to build up monthly synoptic temperature and salinity dataset for January 1990 to December 2009 on 1°×1° grids and the same 33 vertical levels as the World Ocean Atlas. Then, the monthly varying upper layer OHC field (H) was obtained. Second, a composite analysis was conducted to obtain the total-time mean OHC field ($\overline{H}$) and the monthly mean OHC variability ($\widetilde{H}$), which is found an order of magnitude smaller than $\widehat{H}$. Third, an empirical orthogonal function (EOF) method is conducted on the residue data ($\widehat{H}$), deviating from $\overline{H}+\widetilde{H}$, in order to obtain interannual variations of the OHC fields for the three oceans. In the Pacific Ocean, the first two EOF modes account for 51.46% and 13.71% of the variance, representing canonical El Nino/La Nina (EOF-1) and pseudo-El Nino/La Nina (i.e., El Nino Modoki; EOF-2) events. In the Indian Ocean, the first two EOF modes account for 24.27% and 20.94% of the variance, representing basin-scale cooling/warming (EOF-1) and Indian Ocean Dipole (EOF-2) events. In the Atlantic Ocean, the first EOF mode accounts for 49.26% of the variance, representing a basin-scale cooling/warming (EOF-1) event. The second EOF mode accounts for 8.83% of the variance. Different from the Pacific and Indian Oceans, there is no zonal dipole mode in the tropical Atlantic Ocean. Fourth, evident lag correlation coefficients are found between the first principal component of the Pacific Ocean and the Southern Oscillation Index with a maximum correlation coefficient (0.68) at 1-month lead of the EOF-1 and between the second principal component of the Indian Ocean and the Dipole Mode Index with maximum values (around 0.53) at 1–2-month advance of the EOF-2. It implies that OHC anomaly contains climate variability signals.

Keywords Dipole Mode Index (DMI) · El Nino · Pseudo-El Nino · Global Temperature and Salinity Profile Program (GTSPP) · Indian Ocean Dipole · Monthly varying global (T, S) field · Optimal spectral decomposition (OSD) · Southern Oscillation Index (SOI) · Upper ocean heat content

1 Introduction

In the past decade, several new coupled ocean–atmosphere phenomena, such as the pseudo-El Nino (or sometimes called El Nino Modoki) and the Indian Ocean Dipole (IOD), were discovered and recognized important in climate variability. The pseudo-El Nino is characterized by warmer sea surface temperature anomalies (SSTA) in the central equatorial Pacific and cooler SSTA in the eastern and western equatorial Pacific (Ashok et al. 2007; Weng et al. 2007), which is different from the El Nino with anomalous warming in eastern equatorial Pacific. El Nino and pseudo-El Nino have different teleconnection patterns. Taking the Atlantic Ocean as an example, less tropical storms and hurricanes occur during El Niño events (see the website: http://ww2010.atmos.uiuc.edu/(Gh)/guides/mtr/hurr/enso.rxml), and more trop-

Responsible Editor: Pierre-Marie Poulain

This article is part of the Topical Collection on *Multiparametric observation and analysis of the Sea*

P. C. Chu (✉)
Department of Oceanography, Naval Postgraduate School, Monterey, CA 93943, USA
e-mail: pcchu@nps.edu

ical storms and hurricanes appear during pseudo-El Nino events (Weng et al. 2007). Ashok et al. (2007) and Weng et al. (2007) described in detail the difference in teleconnections and climate variability between the pseudo-El Nino event in 2004 and El Nino events. The IOD was identified by Saji et al. (1999) and Vinayachandran et al. (1999).

Climate systems are complex. One way to simplify the climate systems is to represent climate variability of atmospheric circulations by teleconnection patterns, such as the Southern Oscillation Index (SOI), representing the El Nino/La Nina events, and the Dipole Mode Index (DMI), representing the IOD events. The SOI was first to utilize equivalent barotropic seesaw in atmospheric pressure between the southeastern tropical Pacific and the Australian–Indonesian regions (Walker and Bliss 1937). A popular formula for calculating the monthly SOI is proposed by the Australian Bureau of Meteorology:

$$s(\tilde{t}_p) = 10 \times \frac{p_{diff}(\tilde{t}_p) - \langle p_{diff} \rangle}{SD(p_{diff})}. \quad (1)$$

Here, p_{diff} is the mean sea level pressure of Tahiti minus that of Dawin for that month; $\langle p_{diff} \rangle$ is the long-term average of p_{diff} for the month in question; and SD(p_{diff}) is the long-term standard deviation of p_{diff} for the month in question. Positive values of the SOI (Fig. 1a) are associated with stronger Pacific trade winds and warmer sea temperatures to the north of Australia.

The DMI (Fig. 1b) was introduced by Saji et al. (1999) to define the strength of the IOD events. It is defined by the difference in SSTA between the tropical western Indian Ocean (10°S–10°N, 50°–70°E) and the tropical southeastern Indian Ocean (10°S–equator, 90°–110°E). During positive IOD events (i.e., positive DMI), a warm SSTA occurs in the western equatorial Indian Ocean, and a cold SSTA appears in the eastern equatorial Indian Ocean ("La Nina-type" in the Indian Ocean), which causes an easterly wind anomaly, and in turn weakens the eastward equatorial jet (EEJ). During negative DMI (i.e., negative IOD events), a cold SSTA occurs in the western equatorial Indian Ocean, and a warm SSTA appears in the eastern equatorial Indian Ocean ("El Nino-type" in the Indian

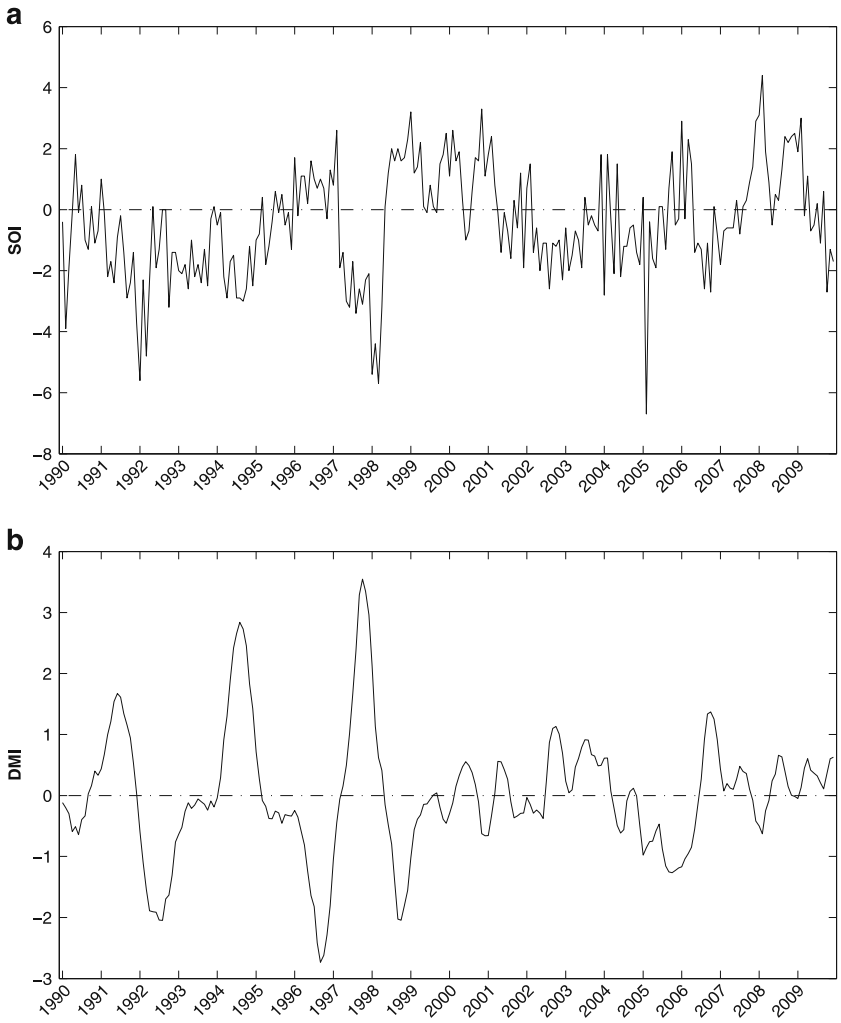

Fig. 1 Time series of **a** SOI and **b** DMI

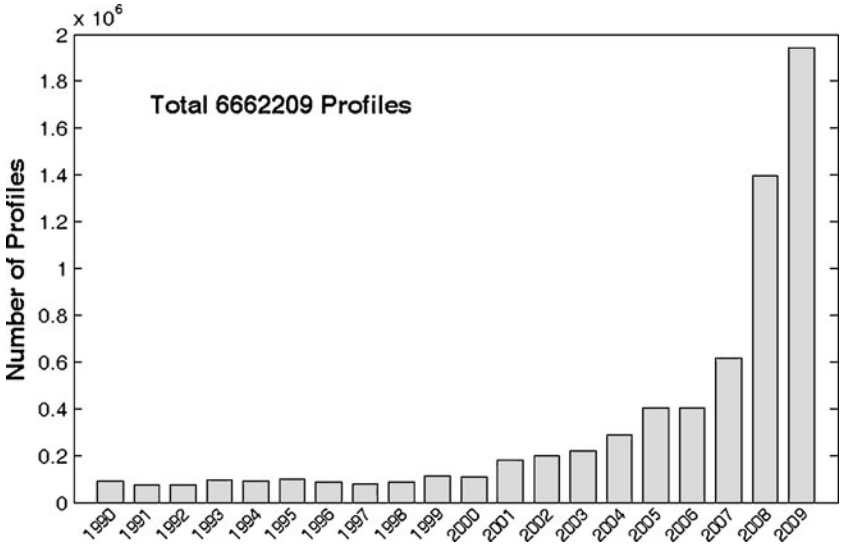

Fig. 2 Temporal distribution of GTSPP stations during 1990–2009 for this study

Ocean), which causes a westerly wind anomaly, and in turn enhances the eastward equatorial jet. Chu (2010) confirmed the relationship between IOD and eastward equatorial jet using observational data.

Upper ocean heat content (OHC) has been recognized important for climate variability. For example, Hasegawa and Hanawa (2003) show the existence of anticlockwise propagation of OHC anomalies in the tropical Northern Pacific, which is related closely to the ENSO events. However, the pseudo-El Nino and IOD events were identified as ocean-atmospheric coupled system from ocean-atmospheric data analysis with SST rather than OHC as a key variable for the ocean. Questions arise: Can the three major tropical systems (ENSO, pseudo-El Nino and IOD) be identified from the

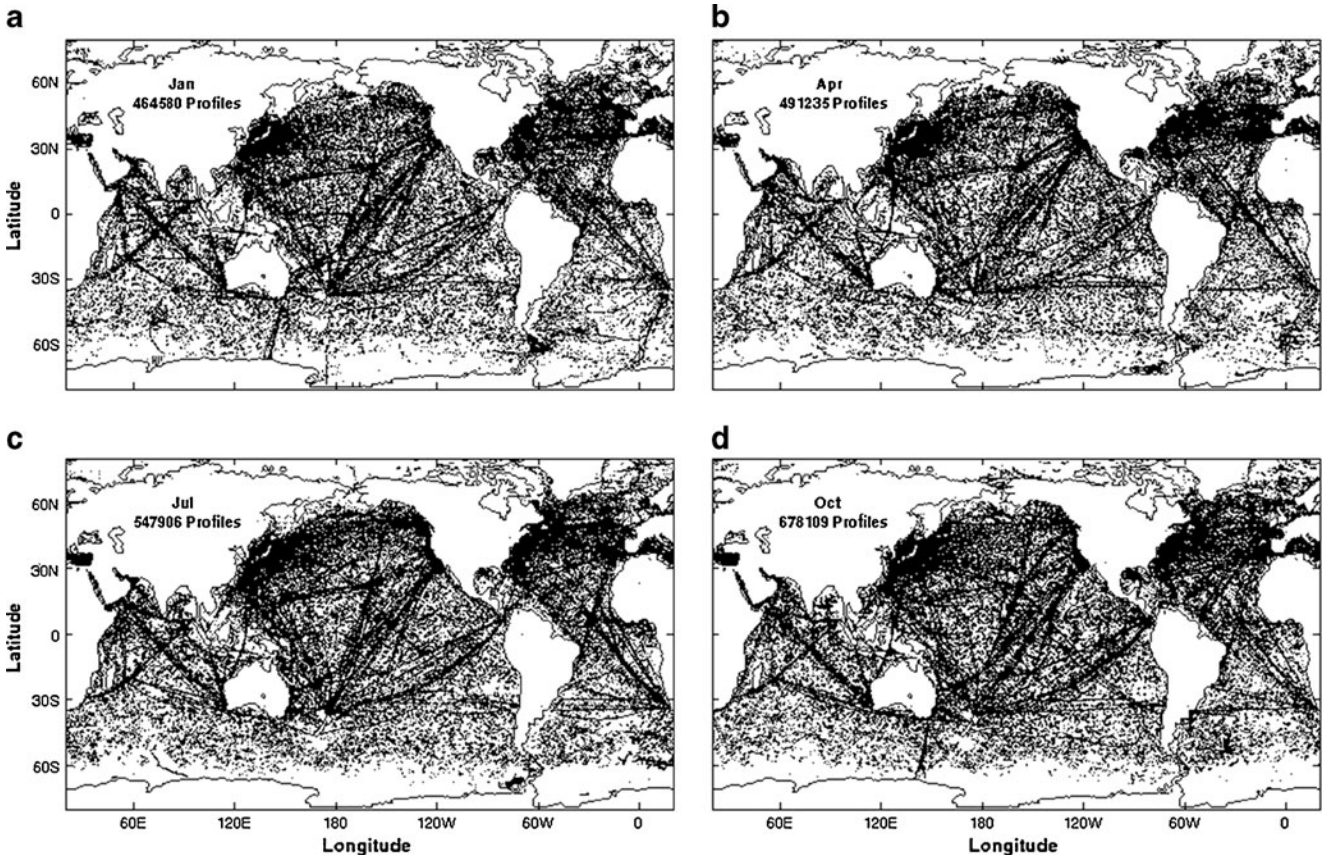

Fig. 3 Spatial distribution of the GTSPP profiles stations during 1990–2009 for **a** January, **b** April, **c** July, and **d** October

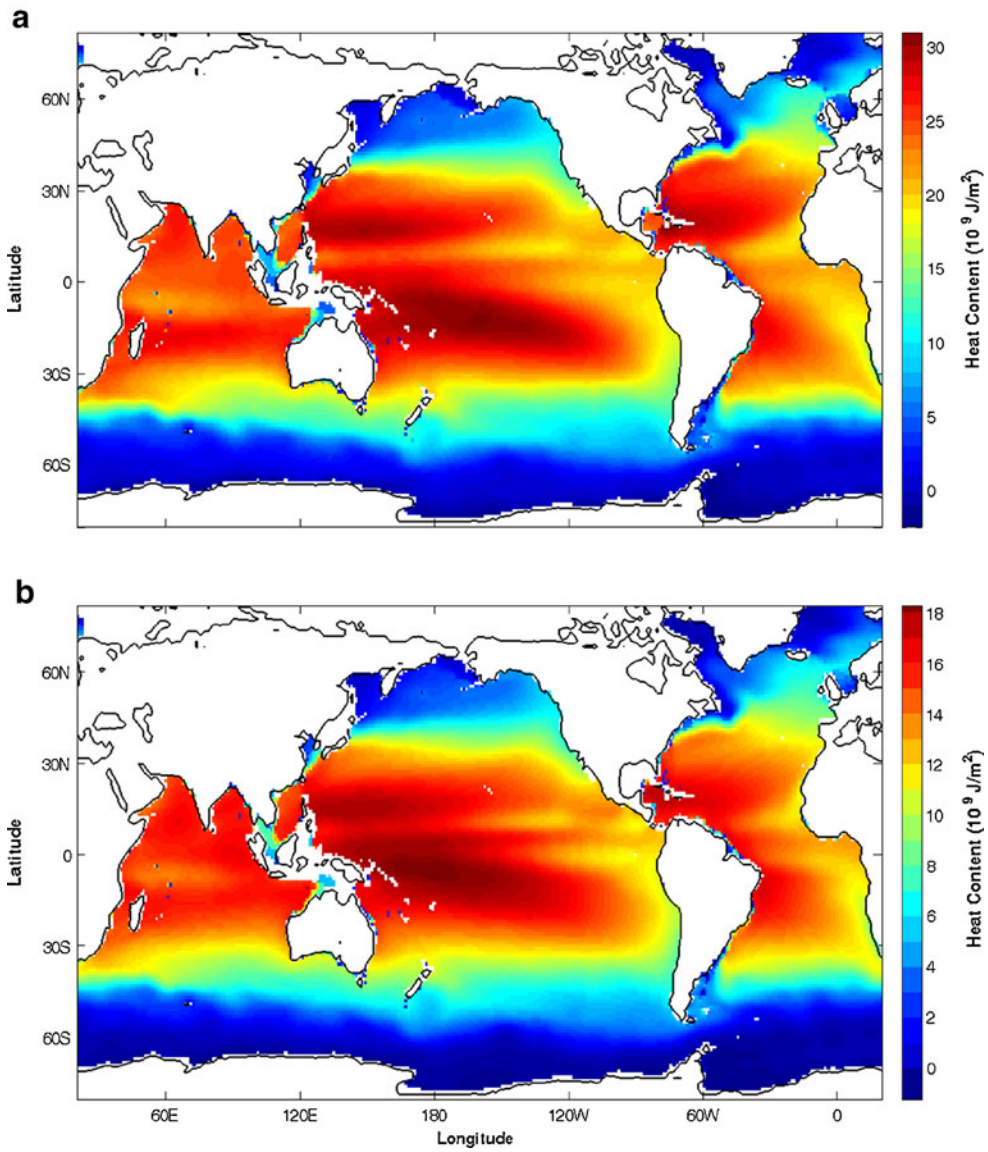

Fig. 4 Total-time mean of global upper ocean heat content during 1990–2009: **a** $\overline{\overline{H}}_{300}(\mathbf{r}_i)$ and **b** $\overline{\overline{H}}_{150}(\mathbf{r}_i)$

upper layer OHC field alone? What are connections between OHC anomaly and climate indices? To answer these questions, an observational dataset from the Global Temperature and Salinity Profile Program (GTSPP) was used. GTSPP has been developed since 1990 with international cooperation (see the website: http://www.iode.org/). With more observed (*T*, *S*) profile data especially with the Argo floats, it is possible to establish gridded (*T*, *S*) dataset with a sufficient resolution in space and, especially, in time using the optimal spectral decomposition (OSD) method (Chu et al. 2003a, b). From the gridded dataset, it is able to compute the upper OHC. The thickness of the upper layer is taken as 300 m for the Pacific/Atlantic Ocean and 150 m for the Indian Ocean since the Indian Ocean has shallower thermoclines. Composite were used to get gridded data of OHC seasonal variability and anomaly.

This paper presents such an effort and is outlined as follows. Section 2 depicts the GTSPP dataset, Section 3 presents characteristics of spatially (1° resolution) and temporally (1-month increment) varying OHC (H:H_{300} for the Pacific/Atlantic Oceans and H_{150} for the Indian Ocean) after using the OSD method, a composite analysis to get the OHC seasonal variability, and an EOF analysis to obtain the OHC anomaly. Sections 4–6 describe temporal and spatial variability of OHC anomaly and the connection to the climate variability. Section 7 lists the conclusions.

2 GTSPP

GTSPP is a cooperative international project. It seeks to develop and maintain a global ocean temperature-salinity

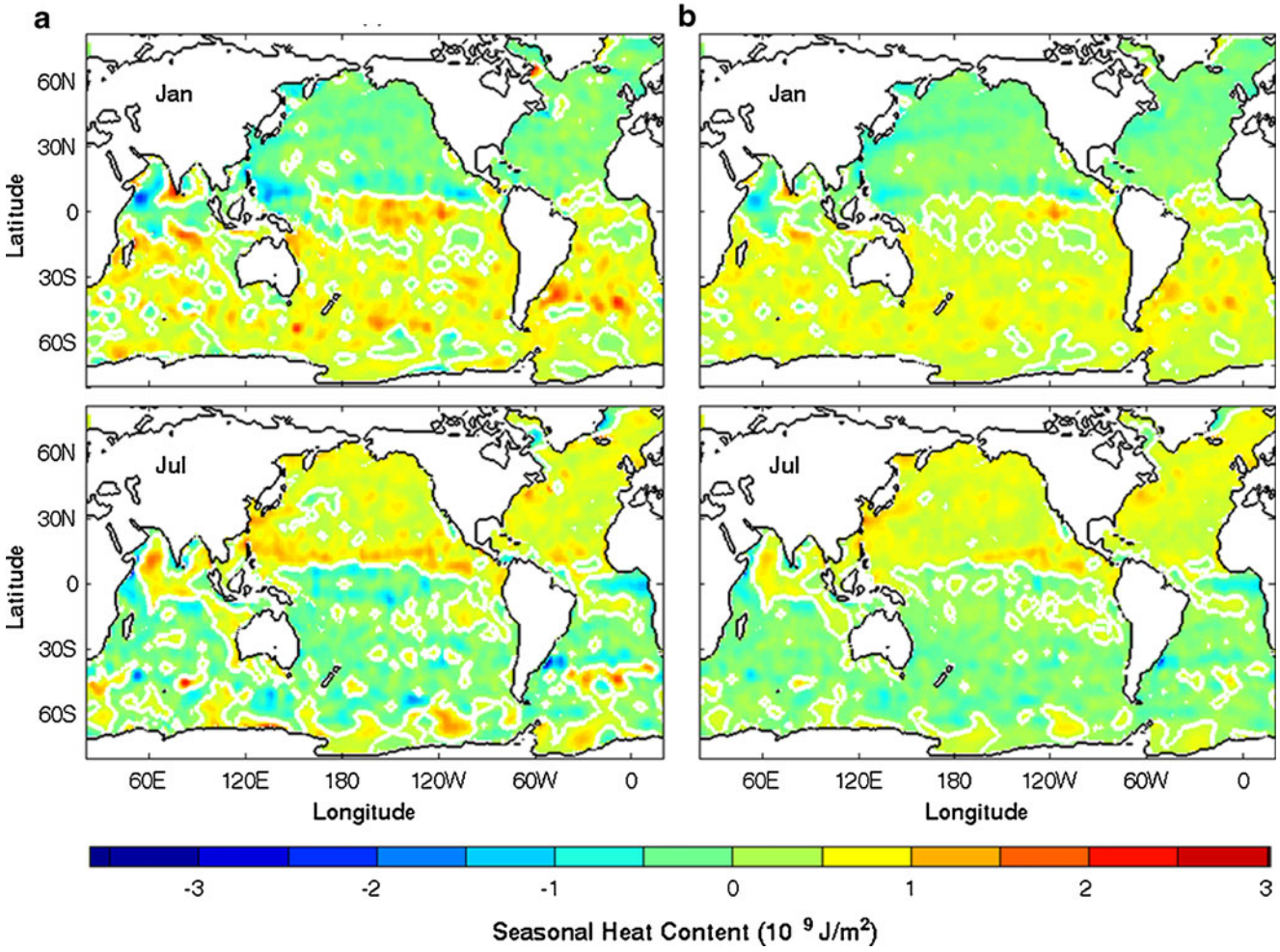

Fig. 5 Mean seasonal variability of upper layer heat content (unit: J/m^2) **a** $\widetilde{\mathrm{H}}_{300}(\mathbf{r}_i, t_l)$ and **b** $\widetilde{\mathrm{H}}_{150}(\mathbf{r}_i, t_l)$, with *upper panels* for January and *lower panels* for July

resource with data that are both up-to-date and of the highest quality possible. Making global measurements of ocean temperature (T) and salinity (S) quickly and easily accessible to users is the primary goal of the GTSPP. Both real-time data transmitted over the Global Telecommunications System and delayed-mode data received by the National Oceanographic Data Center (NODC) are acquired and incorporated into a continuously managed database. The GTSPP handles all temperature and salinity profile data. This includes observations collected using water samplers, continuous profiling instruments such as Argo floats, CTDs, thermistor chain data, and observations acquired using thermosalinographs. The GTSPP went through quality control procedures that make extensive use of flags to indicate data quality. To make full use of this effort, participants of the GTSPP have agreed that data access based on quality flags will be available (Sun et al. 2009). That is, GTSPP participants will permit the selection of data from their archives based on quality flags as well as other criteria. These flags are always included with any data transfers that take place. Because the flags are always included, and because of the policy regarding changes to data, as described later, a user can expect the participants to disseminate data at any stage of processing. Furthermore, GTSPP participants have

Table 1 Variances of the first six leading EOFs of $\widehat{\mathrm{H}}_{300}$ for the Pacific Ocean

EOF	Variance	Cumulative variance
1	0.5146	0.5146
2	0.1371	0.6517
3	0.0644	0.7161
4	0.0473	0.7634
5	0.0375	0.8009
6	0.0307	0.8316

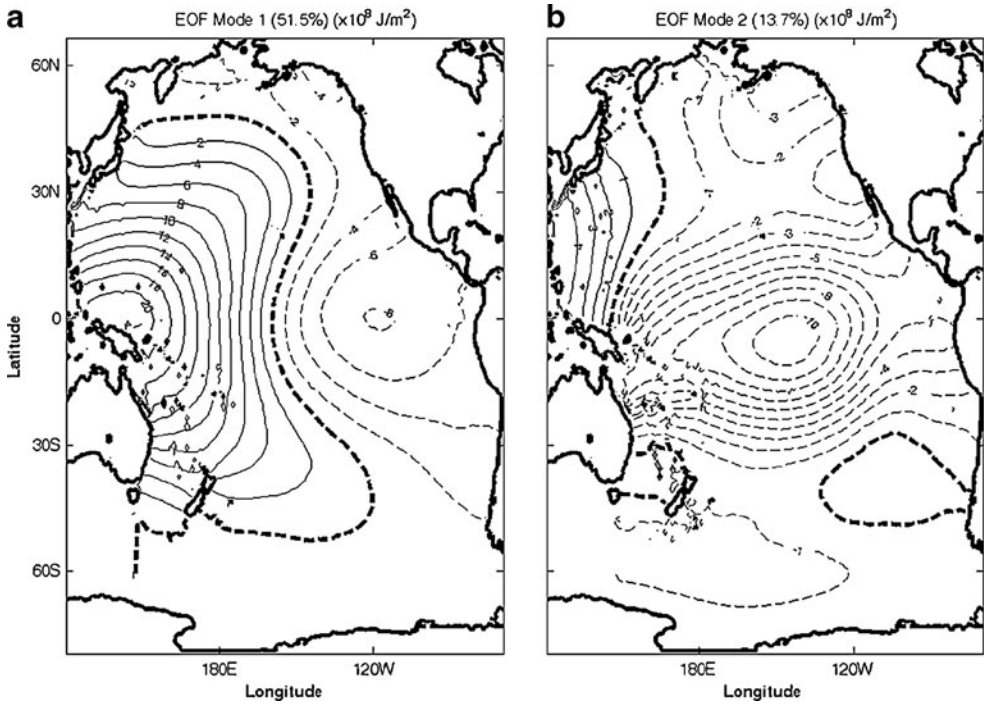

Fig. 6 **a** EOF-1 and **b** EOF-2 of the OHC anomaly $\widehat{H}_{300}$ (unit: 10^8 J/m^2) in the Pacific Ocean

agreed to retain copies of the data as originally received and to make these available to the user if requested (Sun et al. 2009). Interested readers are referred to the following website (http://www.iode.org/) of the International Oceanographic Commission of UNESCO.

There are total 6,662,209 GTSPP stations with temporally increasing data (Fig. 2). The yearly number of (T, S) profiles is less than 80,000 from 1990 to 1999. Since 2000, as the Argo floats into practice, the yearly number of (T, S) profiles increases exponentially close to 1.7 million in 2009. The GTSPP stations are over the global ocean (Fig. 3). The OSD method (see Appendix A) is used to establish 3D global gridded (T, S) dataset with monthly increment, 1°×1° horizontal resolution, and 33 vertical layers as the World Ocean Atlas (http://www.nodc.noaa.gov/OC5/WOA05/pr_woa05.html), which is called as the GTSPP gridded data.

3 Spatial and temporal variability of OHC

3.1 Gridded H_{300} and H_{150} datasets

From the GTSPP gridded dataset, the upper OHC (H) with the unit of J/m^2 is calculated by

$$\mathrm{H}(\mathbf{r}_i, \mathrm{t}_k, t_l) = c_p \int_{-h}^{0} \mathrm{r}\, T dz, h = 150\mathrm{m}, 300\mathrm{m}, \qquad (2)$$

where c_p is the specific heat of the seawater [= 3,850 J/(kg K)]; and ρ is the density, which is calculated from the (T, S) data using the equation of the state; the vectors r_i represent locations of 2D horizontal grids; i=1, 2, …, I, where I is the total number of the horizontal grid points; τ_k=1990, 1991, …, 2009 is the time sequence in years; and t_l=1, 2, …, 12 is the monthly sequence within a year.

3.2 Total-time mean

Before investigating the annual variation of OHC, we define the following two temporal averages:

$$\overline{\mathrm{H}}(\mathbf{r}_i, t_l) = \frac{1}{\Delta \mathrm{t}} \sum_k \mathrm{H}(\mathbf{r}_i, \mathrm{t}_k, t_l), \Delta \mathrm{t} = 20(1990 \text{ to } 2009), \qquad (3a)$$

which are the annual mean values, and

$$\overline{\overline{\mathrm{H}}}(\mathbf{r}_i) = \frac{1}{12} \sum_{l=1}^{12} \overline{\mathrm{H}}(\mathbf{r}_i, t_l), \qquad (3b)$$

which are the total-time mean values. The total-time mean (1990–2009) of global upper ocean heat content with the upper ocean depth of 300 m $\overline{\overline{H}}_{300}(\mathbf{r}_i)$ (Fig. 4a) shows following features: (1) it is usually less than 1.2×10^{10} J/m^2 north of 40°N and south of 40°S. (2) The high $\overline{\overline{H}}_{300}(\mathbf{r}_i)$areas are associated with the subtropical gyres in the Atlantic and Pacific Oceans. For example, in the Atlantic Ocean, a strong warm core (3.0×10^{10} J/m^2) is located in the Gulf Stream region. It extends northeastward and reaches the northwest African Coast. Another warm area (2.8×10^{10} J/m^2) is located in the South Atlantic with a triangular shape from the

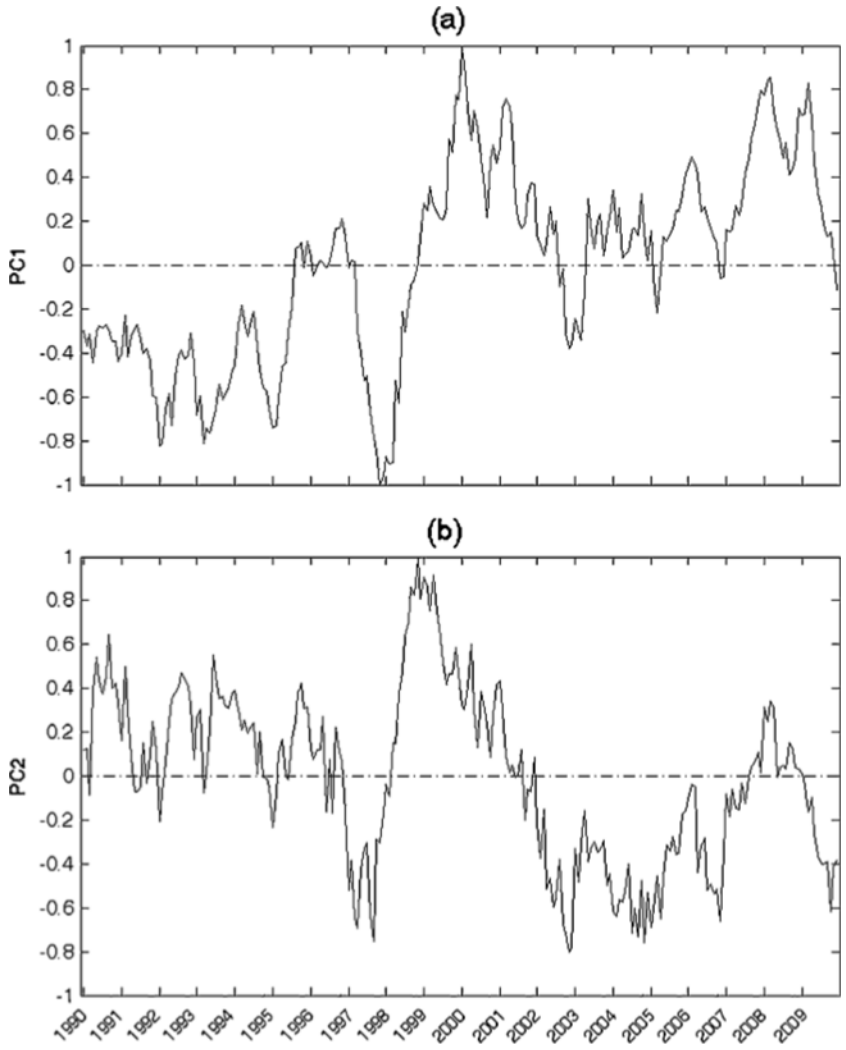

Fig. 7 Time series of principal components for the **a** EOF-1 and **b** EOF-2 modes of the OHC anomaly $\widehat{\mathrm{H}}_{300}$ in the Pacific Ocean

Brazilian-Argentine Coast (15°S to 40°S) to the southwest African Coast (around 40°S). Between the two warm regions, there is a cool area (1.9×10^{10} J/m^2) including the equatorial region. In the Pacific Ocean, there is a warm core in the western North Pacific (the Kuroshio and its extension regions) and the other in the western equatorial/South Pacific with the values around 3.0×10^{10} J/m^2. The eastern Pacific has less values around 2.0×10^{10} J/m^2. The total-time mean of global upper ocean heat content with the upper ocean depth of 150 m $\overline{\overline{\mathrm{H}}}_{150}(\mathbf{r}_i)$ (Fig. 4b) shows similar features with reduced values of $\overline{\overline{\mathrm{H}}}(\mathbf{r}_i)$.

3.3 Mean seasonal variability

The annual mean values deviated from the total-time mean, $\overline{\overline{\mathrm{H}}}(\mathbf{r}_i)$,

$$\widetilde{\mathrm{H}}(\mathbf{r}_i, t_l) = \overline{\mathrm{H}}(\mathbf{r}_i, t_l) - \overline{\overline{\mathrm{H}}}(\mathbf{r}_i), \tag{4}$$

lead to composite features of the mean seasonal variability. The mean seasonal variability of OHC with upper ocean thickness of 300 m (Fig. 5a) and 150 m (Fig 5b) shows the following features: (1) $\widetilde{\mathrm{H}}_{300}(\mathbf{r}_i, t_l)$, with maximum values around 2.6×10^9 J/m^2 is generally an order of magnitude smaller than the total-time mean $\overline{\overline{\mathrm{H}}}_{300}(\mathbf{r}_i)$. Such a feature also exists in $\widetilde{\mathrm{H}}_{150}(\mathbf{r}_i, t_l)$. (2) Its positive values show eddy-like structure, and negative values are more spatially uniform. (3) Usually, negative (positive) values occur in the northern (southern) hemisphere in boreal winter (upper panels in Fig. 5), and positive (negative) values occur in the northern (southern) hemisphere in boreal summer (lower panels in Fig. 5).

3.4 OHC anomaly

OHC anomaly is the deviation from its annual mean value

$$\widehat{\mathrm{H}}(\mathbf{r}_i, \mathbf{t}_k, t_l) = \mathrm{H}(\mathbf{r}_i, \mathbf{t}_k, t_l) - \overline{\mathrm{H}}(\mathbf{r}_i, t_l), \tag{5}$$

which is rearranged into a $N\times P$ matrix, $\widehat{\mathrm{H}}(\mathbf{r}_i, \widetilde{t}_p)$, p=1, 2, …, P. Here, P=240 is the total number of months (i.e.,

total time points). The empirical orthogonal function (EOF) analysis was conducted on the heat content anomaly data

$$\widehat{\mathrm{H}}(\mathbf{r}_i,\widetilde{t}_p)=\sum_j PC_j(\widetilde{t}_p)E_j(\mathbf{r}_i), \tag{6}$$

where $E_j(\mathrm{r_i})$ is the jth EOF mode with the unit of J/m^2; and $PC_j(\widetilde{t}_p)$ is the jth principal component without unit. Here, j=1, 2, …, J; J is truncated number of the EOF modes. The EOF analysis was conducted for the individual ocean such as on $\widehat{\mathrm{H}}_{300}(\mathbf{r}_i,\widetilde{t}_p)$ for the Pacific and Atlantic Oceans and on $\widehat{\mathrm{H}}_{150}(\mathbf{r}_i,\widetilde{t}_p)$ for the Indian Ocean.

4 Pacific Ocean

Table 1 shows the variance of $\widehat{\mathrm{H}}_{300}(\mathbf{r}_i,\widetilde{t}_p)$ for the first six EOFs with EOF-1 containing 51.46% of variance and EOF-2 containing 13.71% of variance. Here, the effort is concentrated on analyzing the first two EOF modes.

4.1 EOF-1 mode

The EOF-1 mode (Fig. 6) shows the positive phase of a zonal dipole structure (i.e., positive–negative): The western Pacific (near half of the Pacific Ocean) is positive with a strong maximum center located at the western tropical Pacific warm pool region north of New Guinea with maximum value higher than 2.0×10^9 J/m^2. The eastern Pacific is negative with minimum value lower than -0.8×10^9 J/m^2 located in the east equatorial Pacific.

The first principal component for 1990–2009, $PC_1(\widetilde{t}_p)$, fluctuates between −1 and 1, which makes the magnitude of the EOF-1 pattern around 2.0×10^9 J/m^2, comparable to the magnitude of the seasonal variability (2.6×10^9 J/m^2). It has an evident upward trend from $PC_1(\widetilde{t}_p)$ generally negative before 1998 to $PC_1(\widetilde{t}_p)$ generally positive after 1999 except 2002 (Fig. 7a). For $PC_1(\widetilde{t}_p)>0$, the horizontal variability of OHC anomaly shows the positive phase (Fig. 6a), representing the La Nina events. For $PC_1(\widetilde{t}_p)<0$, the horizontal variability of OHC anomaly shows the negative phase, representing the El Nino events. The values of $PC_1(\widetilde{t}_p)$ are generally negative in 1990–1998. During this period, $PC_1(\widetilde{t}_p)$ has minimum value in 1991–1992, 1993, 1995, and 1997–1998. They correspond to 1991–1995 long El Nino event, and 1997–1998 El Nino event. The values of $PC_1(\widetilde{t}_p)$ are positive in 1999–2009, which implies that there is no El Nino event (in the classical sense) during this period. Taking 1997–1998 El Nino event as an example, $PC_1(\widetilde{t}_p)$ is −1.0 in November 1997. The OHC has warm anomaly greater than 0.80×10^9 J/m^2 in the eastern Pacific, and cold anomaly in the western Pacific.

4.2 EOF-2 mode

The EOF-2 mode (Fig. 6b) shows the positive phase of a different zonal structure: Small portion of the western Pacific Ocean is positive with a maximum (around 0.45×10^9 J/m^2) located near the Indonesian islands. The rest of the Pacific Ocean is negative with a minimum value around -1.0×10^9 J/m^2 appearing in the equatorial central Pacific (130°W–120°W, 3°N–3°S). The second principal component, $PC_2(\widetilde{t}_p)$, fluctuates between −1 and 1 during 1990–2009, which makes the magnitude of the EOF-2 pattern around 1.0×10^9 J/m^2, a little smaller than the magnitude of the seasonal variability (2.6×10^9 J/m^2). Different from $PC_1(\widetilde{t}_p)$, the second principal component, $PC_2(\widetilde{t}_p)$, does not have a trend (Fig. 7b). For $PC_2(\widetilde{t}_p)>0$, the horizontal variability of OHC anomaly shows the positive phase, representing the La Nina event. For $PC_2(\widetilde{t}_p)<0$, the horizontal variability of OHC anomaly shows the negative phase (i.e., opposite as shown in Fig. 6b). That is, negative OHC anomalies occupy the small portion of the western Pacific Ocean; positive OHC anomalies occupy rest of the oceans with warmest anomaly in the central Pacific Ocean, representing the pseudo-El Nino events. The values of $PC_2(\widetilde{t}_p)$ were negative in short periods in 1992, 1993, and 1996, January 1997 to July 1998, March 2002 to February 2007, and the whole year of 2009. Among them, the period of January

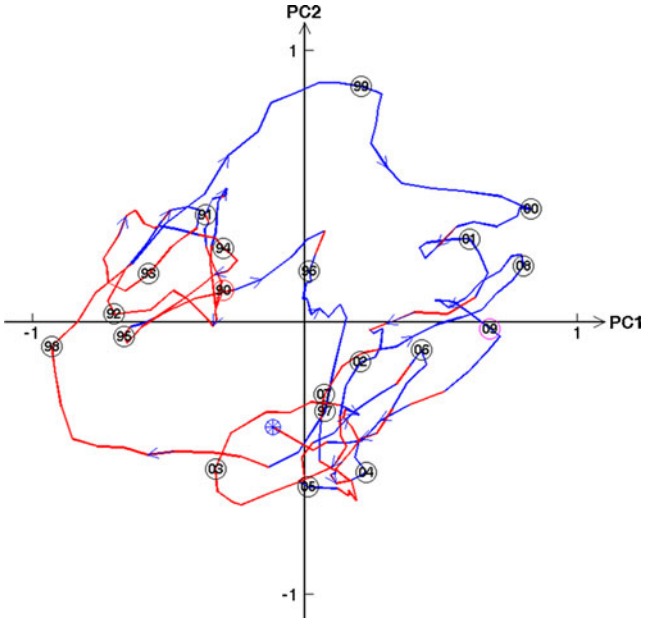

Fig. 8 Trajectory in the phase space (PC_1, PC_2) of the OHC anomaly $\widehat{\mathrm{H}}_{300}$ in the Pacific Ocean from January 1990 to December 2009 (*a star enclosed by a circle*). Here, the *number enclosed by a circle* denotes January of the year (90 means 1990, …); the *arrows* show the time advancement; the *red color* refers to negative values of SOI; and *blue color* refers to positive values of SOI. It is noted that both positive (blue) and negative (red) SOI are found in all four quadrants

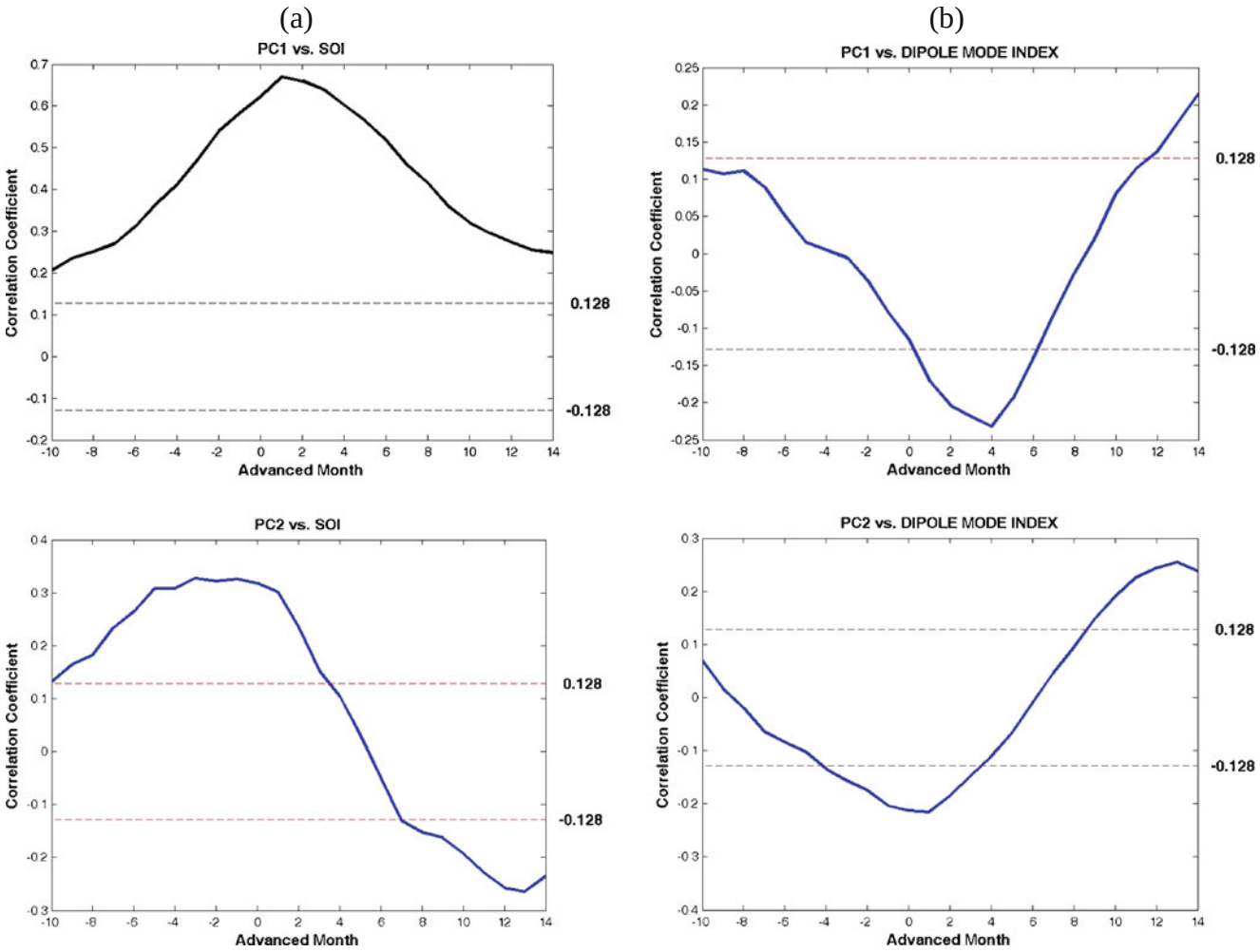

Fig. 9 Lag correlation coefficients between **a** SOI and **b** DMI with PC_1 (*upper panels*) and PC_2 (*lower panels*) of the OHC anomaly $\widehat{H}_{300}$ in the Pacific Ocean with positive time denoting lag of SOI and DMI. It shows evident correlation between SOI and PC_1 with 1-month advance of PC_1, weak correlation between SOI and PC_2 with no-lag to 3-month lag of $PC_2(\widetilde{t}_p)$ to SOI, and no correlation between DMI and (PC_1, PC_2). Here, the *two dashed lines* show the critical values for significant lag-correlation with the significant level of 0.05

1997 to July 1998 is very special, when both $PC_1(\widetilde{t}_p)$ and $PC_2(\widetilde{t}_p)$ are negative, which implies coexistence of an El Nino event from the EOF-1 and a pseudo-El Nino event from the EOF-2. Furthermore, the value of $PC_2(\widetilde{t}_p)$ is −1.0 in October 1997. The OHC of the EOF-2 mode has warm anomaly greater than 1.0×10^9 J/m^2 in the central Pacific; cold anomalies in the western Pacific have a minimum around -0.45×10^9 J/m^2 near Indonesian islands.

4.3 Phase space trajectory

Temporal variation of the two modes can also be represented by the phase diagram with PC_1 as the horizontal axis and PC_2 as the vertical axis (Fig. 8). The trajectory in the phase space starts from January 1990 to December 2009 (a star enclosed by a circle). The number enclosed by a circle denotes January of the year (90 means 1990, …); the arrows show the time advancement; the red color refers to negative values of SOI, and blue color refers to positive values of SOI. The trajectory represents evolution of the OHC anomaly in various phases relating to climate variability. It is noted that both positive (blue) and negative (red) SOI are found in all four quadrants.

For the trajectories between two consecutive years in the quadrant of (+, +) such as 99–00–01 (representing January

Table 2 Variances of the first six leading EOFs of $\widehat{H}_{150}$ for the Indian Ocean

EOF	Variance	Cumulative variance
1	0.2427	0.2427
2	0.2094	0.4521
3	0.1172	0.5648
4	0.1107	0.6755
5	0.0548	0.7303
6	0.0475	0.7778

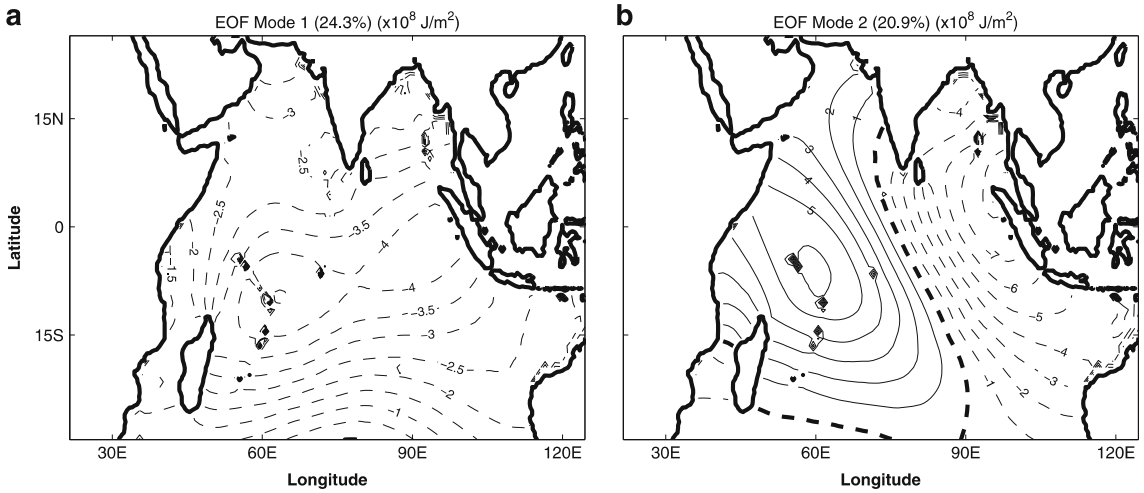

Fig. 10 **a** EOF-1 and **b** EOF-2 of the OHC anomaly $\widehat{H}_{150}$ (unit: 10^8 J/m^2) in the Indian Ocean. It is noted that the EOF-1 mode represents basin-scale warming/cooling, and the EOF-2 mode represents the dipole mode

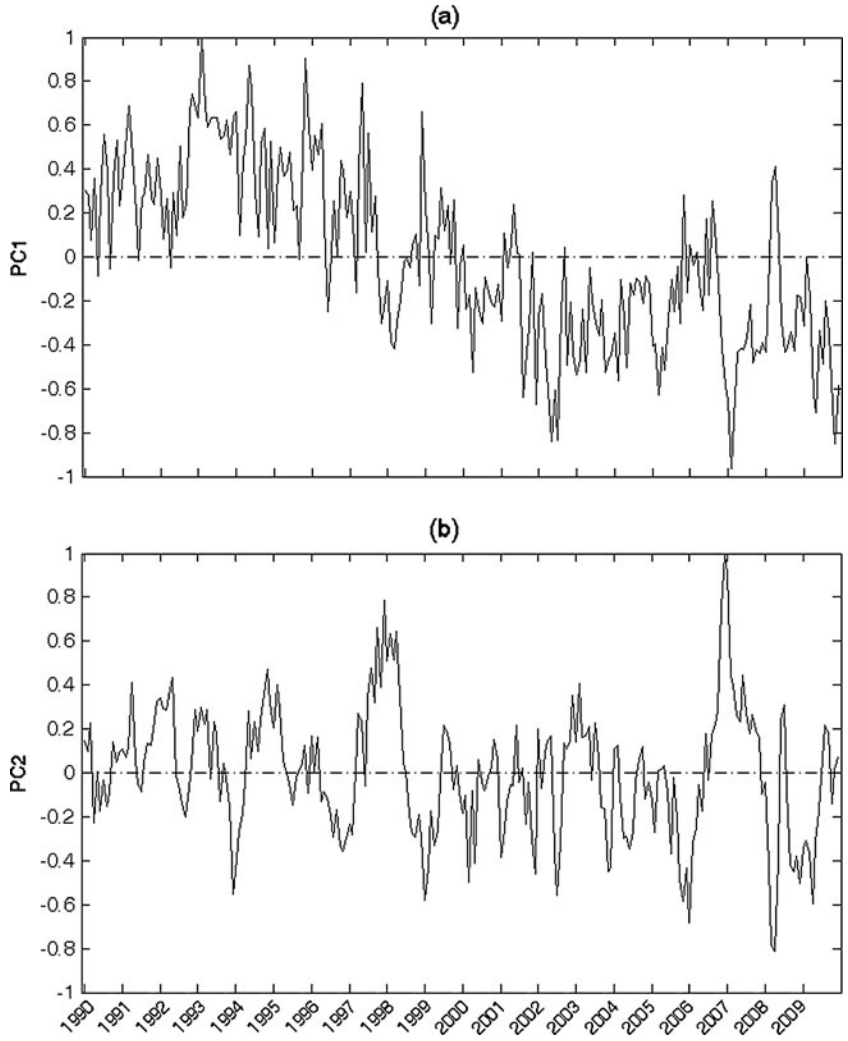

Fig. 11 Time series of principal components for the **a** EOF-1 and **b** EOF-2 modes of the OHC anomaly $\widehat{H}_{150}$ in the Indian Ocean

1999 to January 2001), 08–09 (representing January 2008 to January 2009), both EOF-1 and EOF-2 modes are in the positive phase, implying strong La Nina in the tropical Pacific. For the trajectories between two consecutive years in the quadrant of (−, −) such as March 97–January 98, both EOF-1 and EOF-2 modes are in the negative phase, which implies coexistence of El Nino and pseudo-El Nino in the tropical Pacific. For the trajectories between two consecutive years in the quadrant of (+, −) such as 04–05–06–07, and most months in 2009, the EOF-1 mode is in the positive phase, and the EOF-2 mode is in the negative phase, which implies pseudo-El Nino in the tropical Pacific. For the trajectories between two consecutive years in the quadrant of (−, +) such as most months in 1990–1995, the EOF-1 mode is in the negative phase, and the EOF-2 mode is in the positive phase or near zero such as 92 and 95, which implies El Nino in the tropical Pacific.

4.4 Lag correlations between (SOI, DMI) and principal components

Linkage between the OHC anomaly in the Pacific Ocean and climate variability is represented by the lag-correlation coefficients between the (SOI, DMI) with the principal components $PC_1(\tilde{t}_p)$ and $PC_2(\tilde{t}_p)$. The total size of the time series (n) is 240 (20 years of monthly data between 1990 and 2009) for the no-lag correlation coefficients. For an l-month lag correlation, the data size is $(n-l)$.

The lag-correlation coefficients show strong association between $PC_1(\tilde{t}_p)$ and $s(\tilde{t}_p)$ with a maximum values around 0.68 with 1-month advance of PC_1 (Fig. 9a, upper panel), weak association between $PC_2(\tilde{t}_p)$ and $s(\tilde{t}_p)$ with maximum values around 0.32 with no-lag to 3-month lag of $PC_2(\tilde{t}_p)$ to $s(\tilde{t}_p)$ (Fig. 9a, lower panel), and no association between DMI and (PC_1, PC_2) (Fig. 9b). This suggests that the EOF-1 mode is strongly related to the Southern Oscillation with a maximum correlation at 1-month lead of the EOF-1; and the EOF-2 mode (pseudo El Nino) is related weakly to the Southern Oscillation with a maximum correlation at no-lag to 3-month lag of the EOF-2.

5 Indian Ocean

Table 2 shows the variance of $\widehat{\mathrm{H}}_{150}(\mathbf{r}_i, \tilde{t}_p)$ for the first six EOFs with EOF-1 containing 24.27% of variance and EOF-2 containing 20.94% of variance. Here, the effort is concentrated on analyzing the first 2 EOF modes.

5.1 EOF-1 mode

The EOF-1 mode (Fig. 10a) shows a basin-scale cooling/warming (i.e., basin-scale mode) with the positive phase depicted as the basin-scale cooling with a strong cooling zone stretching from northeast of Madagascar to the west coast of Sumatera with minimum value lower than -0.45×10^9 J/m^2 in the west near the Mascarene Plateau. The cooling weakens away from this strong cooling zone with value around -0.1×10^9 J/m^2 near 30°S.

The first principal component for 1990–2009,$PC_1(\tilde{t}_p)$, fluctuates between −1 and 1, which makes the amplitude of the EOF-1 pattern around 0.45×10^9 J/m^2 (Fig. 11a). This value is only 17% of the magnitude of the seasonal variability (2.6×10^9 J/m^2). Moreover, $PC_1(\tilde{t}_p)$ has an evident downward trend from generally positive values (basin-scale cooling) before 2000 (except 1997–1998) with a maximum value of +1.0 in November 1992 to generally negative values (basin-scale warming) after 2000 with a minimum value of −0.98 in November 2007.

5.2 EOF-2 mode

The EOF-2 mode (Fig. 10b) shows the positive phase of a zonal dipole structure (i.e., positive–negative): The western Indian Ocean (near half of the Indian Ocean) is positive with a warm center (higher than 0.6×10^9 J/m^2) located northeast of Madagascar. The eastern Indian Ocean is negative with cool center (lower than -0.8×10^9 J/m^2) located west of Sumatera. This pattern corresponds to the

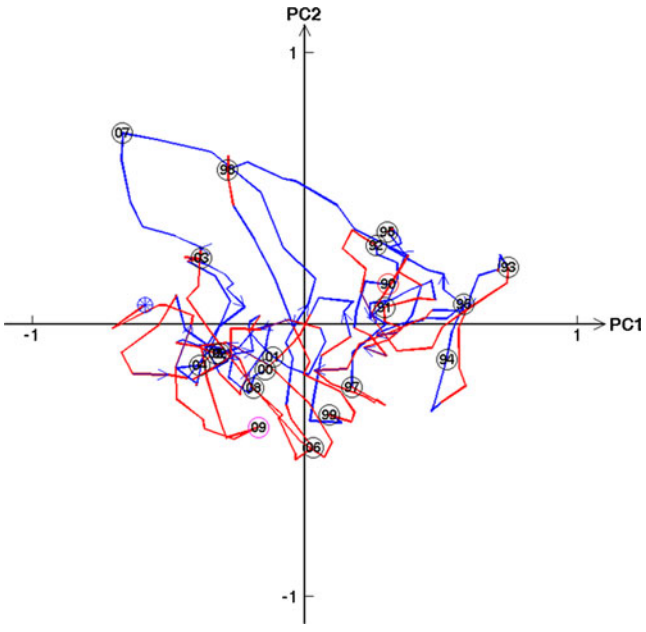

Fig. 12 Trajectory in the phase space (PC_1, PC_2) of the OHC anomaly $PC_1(\tilde{t}_p)$ in the Indian Ocean from January 1990 to December 2009 (*a star enclosed by a circle*). Here, the *number enclosed by a circle* denotes January of the year (90 means 1990, ...); the *arrows* show the time advancement; the *red color* refers to negative values of DMI and *blue color* refers to positive values of DMI. It is noted that both positive (*blue*) and negative (*red*) DMI are found in all four quadrants, but more in the third and fourth quadrants

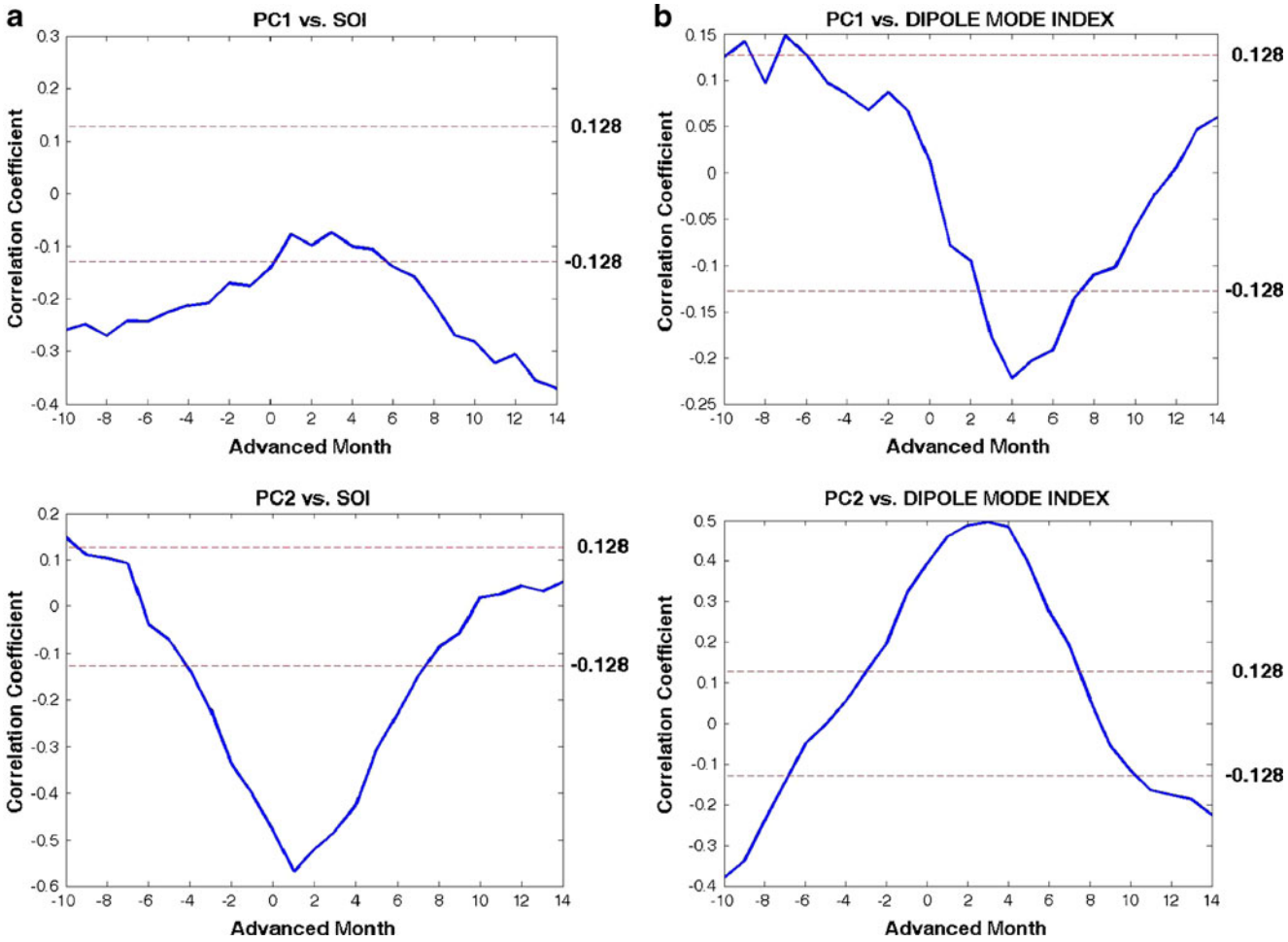

Fig. 13 Lag correlation coefficients between **a** SOI and **b** DMI with PC_1 (*upper panels*) and PC_2 (*lower panels*) of the OHC anomaly $\widehat{H}_{150}$ in the Indian Ocean with positive time denoting lag of SOI and DMI. It shows no correlation between (SOI, DMI) and PC_1, evident negative correlation between SOI and PC_2 with 1-month advance of PC_2, and evident positive correlation between DMI and PC_2 with 2-month advance of PC_2. Here, the *two dashed lines* show the critical values for significant lag-correlation with the significant level of 0.05

positive IOD event, and similar to the pattern obtained from the ocean-atmospheric coupled mode (Rao et al. 2002).

The second principal component $PC_2(\widetilde{t}_p)$, fluctuates between −1 and 1 during 1990–2009, which makes the amplitude of the EOF-2 pattern around 0.8×10^9 J/m^2, smaller than the magnitude of the seasonal variability (2.6×10^9 J/m^2). Different from $PC_1(\widetilde{t}_p)$, the second principal component, $PC_2(\widetilde{t}_p)$, does not have a trend (Fig. 11b). For $PC_2(\widetilde{t}_p) > 0$, the horizontal variability of OHC anomaly shows the positive phase (i.e., the positive IOD event): The western Indian Ocean is positive with a warm center located northeast of Madagascar; and the eastern Indian Ocean is negative with a cool center located west of Sumatera. For $PC_2(\widetilde{t}_p) < 0$, the horizontal variability of OHC anomaly shows the negative phase (i.e., the negative IOD event): The western Indian Ocean is negative with a cool center located northeast of Madagascar; and the eastern Indian Ocean is positive with a warm center located west of Sumatera, representing the negative IOD event. Generally, $PC_2(\widetilde{t}_p)$, shows more frequent occurrence of positive values before 2000 than after 2000: 1991, 1992, 1993, 1994–1995, 1997–1998, 2003–2004, and 2006–2008. Among them, the events of 1994, 1997, 2003, and 2006 are significant. The period of January 1997 to July 1998 is very special, and the positive IOD event [positive $PC_2(\widetilde{t}_p)$ for the Indian Ocean] is coexistence with El Nino

Table 3 Variances of the first six leading EOFs of $\widehat{H}_{300}$ for the Atlantic Ocean

EOF	Variance	Cumulative variance
1	0.4926	0.4926
2	0.0883	0.5809
3	0.0561	0.6370
4	0.0514	0.6884
5	0.0401	0.7285
6	0.0362	0.7647

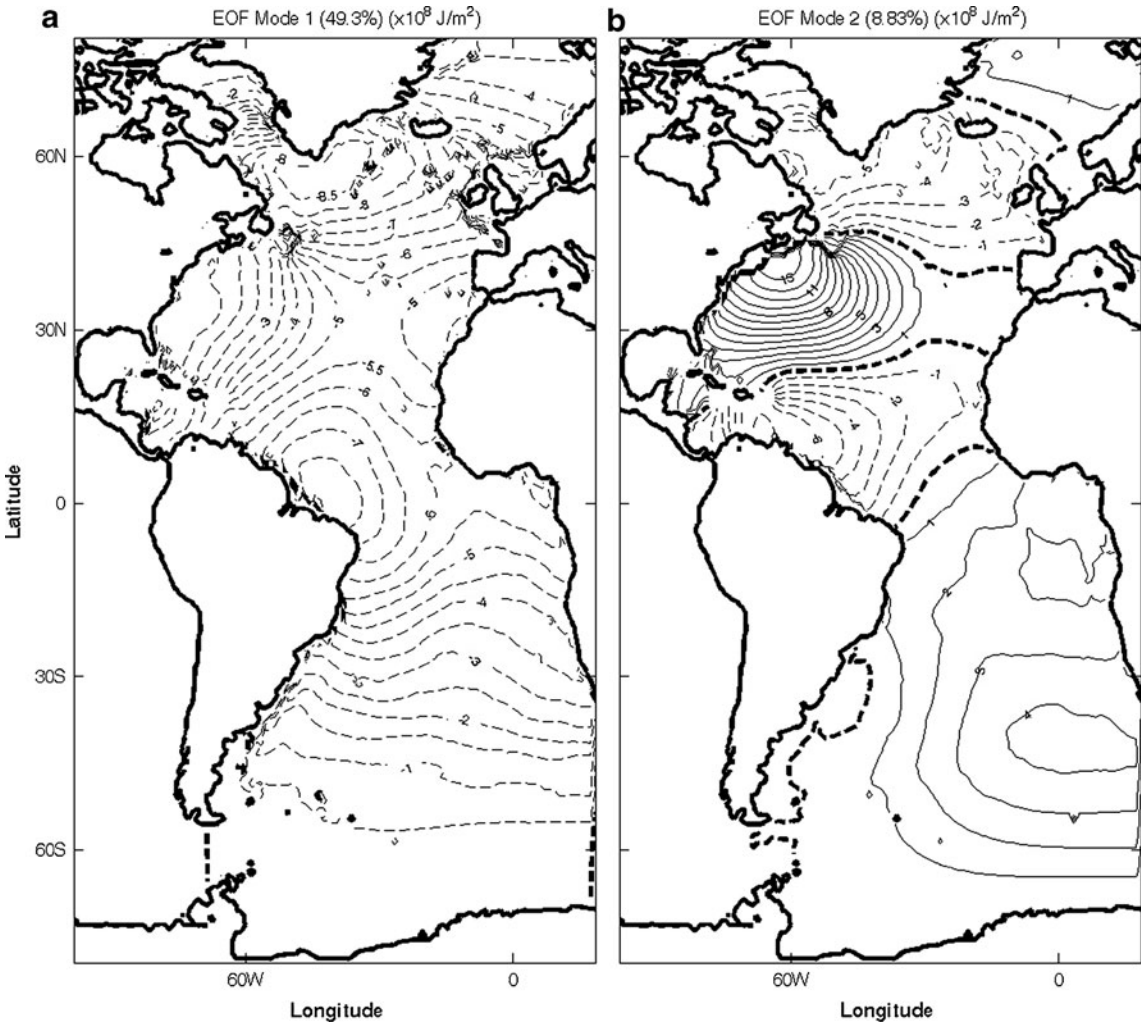

Fig. 14 **a** EOF-1 and **b** EOF-2 of the OHC anomaly $\widehat{H}_{300}$ (unit: 10^8 J/m^2) in the Atlantic Ocean. It is noted that there is no zonal dipole pattern in the EOF-1 and EOF-2 modes

event [negative $PC_1(\widetilde{t}_p)$ for the Pacific Ocean] and pseudo-El Nino event [negative $PC_2(\widetilde{t}_p)$ for the Pacific Ocean].

5.3 Phase space trajectory

Temporal variation of the two modes can also be represented by the phase diagram with PC_1 as the horizontal axis and PC_2 as the vertical axis (Fig. 10). The trajectory in the phase space starts from January 1990 to December 2009 (a star enclosed by a circle). The number enclosed by a circle denotes January of the year (90 means 1990, …); the arrows show the time advancement; the red color refers to negative values of DMI and blue color refers to positive values of DMI. The trajectory represents evolution of the OHC anomaly in various phases relating to climate variability. It is noted that both positive (blue) and negative (red) DMI are found in all four quadrants and the phase space trajectory is more chaotic for the Indian Ocean (Fig. 12) than for the Pacific Ocean (Fig. 8). Such different behaviors in the phase space trajectories need to be further investigated using a numerical model, which is beyond the scope of this study.

5.4 Lag correlations between (SOI, DMI) and principal components

Linkage between the OHC anomaly in the Indian Ocean and climate variability is represented by the lag-correlation coefficients between (SOI, DMI) and the principal components $PC_1(\widetilde{t}_p)$ and $PC_2(\widetilde{t}_p)$. The lag-correlation coefficients show no association between $PC_1(\widetilde{t}_p)$ and (SOI, DMI) (Fig. 13a, b, upper panels), evident negative association between $PC_2(\widetilde{t}_p)$ and SOI with a minimum value of −0.57 for 1-month lead of$PC_2(\widetilde{t}_p)$, and evident positive association between $PC_2(\widetilde{t}_p)$ and DMI with a maximum value around 0.52 for 2-month advance of $PC_2(\widetilde{t}_p)$ to $s(\widetilde{t}_p)$ (Fig. 13a, b, lower panels). This clearly shows the coexistence of the

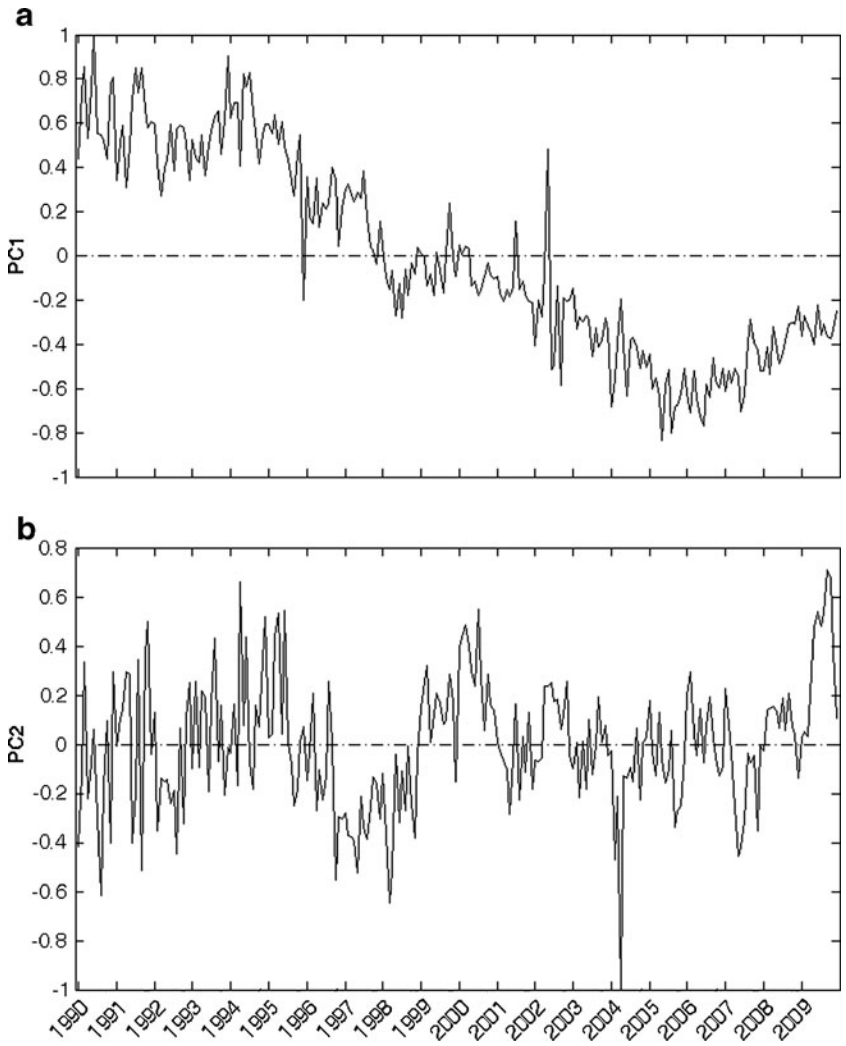

Fig. 15 Time series of principal components for the **a** EOF-1 and **b** EOF-2 modes of the OHC anomaly $PC_2(\widetilde{t}_p)$, in the Atlantic Ocean

positive phase of the EOF-2 mode, the negative phase of SOI (El Nino events), and the positive IOD events.

6 Atlantic Ocean

Table 3 shows the variance of $\widehat{\mathrm{H}}_{300}(\mathbf{r}_i, \widetilde{t}_p)$ for the first six EOFs with EOF-1 containing 49.26% of variance and EOF-2 containing 8.83% of variance. Here, the effort is concentrated on analyzing the first 2 EOF modes.

6.1 EOF-1 mode

The EOF-1 mode (Fig. 14a) shows a positive phase of the basin-scale mode (showing basin-scale cooling) with two strong and two weak cooling zones. The two strong cooling zones with minimum values lower than -0.8×10^9 J/m^2 are located at the tropics (15°S–15°N) near Brazilian coast and high latitudes (50°N–65°N) near Greenland. The two weak cooling zones are located at the mid-latitudes (15°N–50°N) with minimum values around -0.1×10^9 J/m^2 in the western part near the US coasts and around -0.4×10^9 J/m^2 in eastern parts near the northwest African coast. The EOF-1 contours nearly follow the latitudes in the South Atlantic Ocean with reduction of variability southward.

The first principal component for 1990–2009, $PC_1(\widetilde{t}_p)$, fluctuates between −1 and 1, which makes the amplitude of the EOF-1 pattern around 0.8×10^9 J/m^2 (Fig. 15a). This value is smaller than the magnitude of the seasonal variability (~2.5×10^9 J/m^2, see Fig. 5). Moreover, $PC_1(\widetilde{t}_p)$ has an evident downward trend from generally positive values (basin-scale cooling) before 2000 (except 1997–1998) with a maximum value of +1.0 in April 1990 to generally negative values (basin-scale warming) after 2000 except 2002 with a minimum value of −0.83 in March 2005.

6.2 EOF-2 mode

The EOF-2 mode (Fig. 14b) shows the positive phase of latitudinal alternative cooling/warming zones: The South

Atlantic is positive with a warm center (higher than 0.4×10^9 J/m^2) located in the southeast part. The tropical North Atlantic Ocean (0°–25°N) is generally negative with a cold center (lower than -0.6×10^9 J/m^2) near Brazilian coast. The mid-latitude North Atlantic Ocean (25°–50°N) is generally positive with a warm center (higher than 1.3×10^9 J/m^2) near Newfoundland, Canada. The high-latitude North Atlantic Ocean (north of about 50°N) is generally negative with a cold center (lower than -0.5×10^9 J/m^2) near Greenland. The second principal component $PC_2(\tilde{t}_p)$, fluctuates between −1 and 0.72 during 1990–2009, with no evident trend. Since the EOF-2 mode only contains 8.83% of the total variability, it will not be discussed here.

7 Conclusions

The major goal of this study was to identify the interannual variability in the upper OHC anomaly and its relationship to climate change. A 3D global gridded (T, S) dataset has been established with monthly increment, 1°×1° horizontal resolution, and 33 vertical layers as the World Ocean Atlas (http://www.nodc.noaa.gov/OC5/WOA05/pr_woa05.html) from the GTSPP data using the OSD method. The upper OHC for the global oceans was calculated from the 3D global gridded dataset with the upper layer thickness as 300 m for the Pacific and Atlantic Oceans and as 150 m for the Indian Ocean. The composite and EOF analyses were conducted on the OHC data. The following results were obtained:

1. The total-time mean OHC field ($\overline{\overline{\mathrm{H}}}$) was established with OHC less than 1.2×10^9 J/m^2 north of 40°N and south of 40°S. The high $\overline{\overline{\mathrm{H}}}(\mathbf{r}_i)$areas are associated with the subtropical gyres in the Atlantic and Pacific Oceans with OHC ranging from 2.8 to 3.0×10^{10} J/m^2. The OHC is less outside than inside of the subtropical gyres in the same latitudinal zone, such as in the eastern Pacific (around 2.0×10^{10} J/m^2).
2. The composite analysis indicates the following features of the mean seasonal variability of OHC (i.e., annual mean OHC relative to the total-time mean OHC). The maximum seasonal variability is an order of magnitude smaller than the total-time mean $\overline{\overline{\mathrm{H}}}(\mathbf{r}_i)$. Positive variability (summer) shows eddy-like structure, and negative variability (winter) is more spatially uniform.
3. The EOF analysis was conducted to analyze the OHC anomaly data (removal of total-time mean and mean seasonal variability) for the Pacific, Indian, and Atlantic Oceans to identify low-frequency variability of the OHC anomaly. The patterns of the first two EOF modes are different for the three oceans: (a) two zonal modes in the tropical Pacific with the EOF-1 (51.46% variance) representing the canonical El Nino/La Nina events, and the EOF-2 (13.71% variance) representing the pseudo El Nino/La Nina events; (b) one zonal mode in the tropical Indian Ocean with the EOF-1 (24.27% variance) representing the basin-scale cooling/warming events, and the EOF-2 (20.94% variance) representing the Indian Ocean Dipole mode; and (c) no zonal model in the tropical Atlantic with the EOF-1 (49.26% variance) representing the basin-scale cooling/warming events, and the EOF-2 (8.83% variance, insignificant mode).
4. In the Pacific Ocean, the EOF-1 mode is strongly related to the Southern Oscillation with a maximum correlation at 1-month lead of the EOF-1; and the EOF-2 mode (pseudo El Nino) is related weakly to the Southern Oscillation with a maximum correlation at no-lag to 3-month lag of the EOF-2. In the Indian Ocean, the EOF-1 mode (basin-scale cooling/warming mode) has no correlation with (SOI, DMI). The EOF-2 mode has evident negative correlation to SOI with a minimum value of −0.57 for 1-month lead of PC_2, and evident positive correlation to DMI with a maximum value around 0.52 for 2-month advance of PC_2. This clearly shows the coexistence of the positive phase of the EOF-2 mode, the negative phase of SOI, and the positive IOD events. This implies that the upper ocean may take a key role in climate variability.

Acknowledgments The Office of Naval Research, the Naval Oceanographic Office, and the Naval Postgraduate School supported this study. The author thanks Dr. Noden E. Huang at the National Central University in Taiwan for stimulating discussion, Dr. L. Charles Sun at NOAA/NODC for providing the GTSPP data, and Mr. Chenwu Fan at NPS for computing assistance.

Appendix A: Optimal spectral decomposition

A new data analysis/assimilation scheme, the optimal spectral decomposition (OSD), has been recently developed to analyze fields from noisy and sparse oceanographic data. Let (x, z) be horizontal and vertical coordinates and t be time. A physical variable $c(\mathbf{x},z,t)$ at depth z_k is decomposed using the generalized Fourier series (Chu 1999; Chu et al. 2003a, b; Chu et al. 2005a, b)

$$c(\mathbf{x},z_k,t)=c_0(z_k,t)+\sum_{m=1}^{M}a_m(z_k,t)\mathsf{6}_m(\mathbf{x},z_k),\ \mathbf{x}\in R(z_k) \qquad (\mathrm{A1})$$

where c_0 is the horizontal mean of the variable c. M is the truncated mode number, and $\mathsf{6}_m(\mathbf{x},z_k)$ and $a_m(z_k,t)$ are the orthogonal basis functions (or called modes) and the spectral coefficients, respectively; $R(z_k)$ is the area bounded

by the lateral boundary $*(z_k)$ at depth z_k. The basis functions $\{6_m(\mathbf{x}, z_k)\}$ are eigen-functions of the horizontal Laplace operator $\left(\nabla_h^2 \equiv \partial^2/\partial x^2 + \partial^2/\partial y^2\right)$ with the basin geometry and certain physical boundary conditions. For temperature and salinity, the homogeneous Neumann boundary condition is taken at the solid boundary $\Gamma(z)$ (i.e., no heat and salt fluxes),

$$\nabla_h^2 6_m = -l_m 6_m, \mathbf{n} \bullet \nabla_h 6_m|_* = 0, m = 1, 2, ..., M, \quad (A2)$$

where n is the unit vector normal to $*(z)$. The basis functions $\{6_m\}$ are independent of the data and therefore available prior to the data analysis. The OSD method has two important procedures: optimal mode truncation and determination of spectral coefficients $\{a_m\}$. The optimal mode truncation (M) is determined using Vapnik (1983) variational method. Application of the generalized Fourier series expansion (1) to the observational points with P as the total number of observations leads to an algebraic equation

$$\mathbf{Aa} = \mathbf{QY} \quad (A3)$$

where $a=(a_1, a_2, \ldots, a_M)$ is the state vector (M-dimensional); A is a $P\times M$ matrix; Q is a $P\times P$ square matrix ($P>M$); Y is a P-dimensional observation vector, consisting of a signal $\mathbf{Y}$ and a noise Y'. Due to high level of noise contained in the observations, the algebraic equation (A3) is ill-posed and needs to be solved by a rotation matrix regularization method (Chu et al. 2004) that provides (a) stability (robustness) even for data with high noise and (b) the ability to filter out errors with a priori unknown statistics. Interested readers are referred to Chu et al. (2003a, b, 2004).

References

Ashok K, Behera S, Rao AS, Weng H, Yamagata T (2007) El Nino Modoki and its teleconnection. J Geophys Res 112:C11007. doi:10.1029/2006JC003798

Chu PC (1999) Fundamental circulation functions for the determination of open boundary conditions. *Third Conference on Coastal Oceanic and Atmospheric Prediction*. American Meteorological Society 389–394

Chu PC (2010) Observational studies on association between eastward equatorial jet and Indian Ocean dipole. J Oceanogr 66:429–434

Chu PC, Ivanov LM, Korzhova TP, Margolina TM, Melnichenko OM (2003a) Analysis of sparse and noisy ocean current data using flow decomposition. Part 1: theory. J Atmos Oceanic Technol 20:478–491

Chu PC, Ivanov LM, Korzhova TP, Margolina TM, Melnichenko OM (2003b) Analysis of sparse and noisy ocean current data using flow decomposition. Part 2: application to Eulerian and Lagrangian data. J Atmos Oceanic Technol 20:492–512

Chu PC, Ivanov LM, Margolina TM (2004) Rotation method for reconstructing process and field from imperfect data. Int J Bifur Chaos 14:2991–2997

Chu PC, Ivanov LM, Melnichenko OM (2005a) Fall-winter current reversals on the Texas-Louisiana continental shelf. J Phys Oceanogr 35:902–910

Chu PC, Ivanov LM, Margolina TM (2005b) Seasonal variability of the Black Sea Chlorophyll-a concentration. J Mar Syst 56:243–261

Hasegawa T, Hanawa K (2003) Heat content related to ENSO variability in the Pacific. J Phys Oceanogr 33:407–421

Rao SA, Behera SK, Masumoto Y and T Yamagata 2002 Interannual subsurface variability in the tropical Indian Ocean with a special emphasis on the Indian Ocean Dipole. Deep–Sea Res. II, 49, 1549–1572

Saji NH, Goswami BN, Vinayachandran PN, Yamagata T (1999) A dipole in the tropical Indian Ocean. Nature 401:360–363

Sun LC, Thresher A, Keeley R et al. 2009 The data management system for the Global Temperature and Salinity Profile Program (GTSPP). In Proceedings of the "OceanObs'09: Sustained Ocean Observations and Information for Society" Conference (Vol. 2), Venice, Italy, 21–25 September 2009, Hall, J, Harrison D.E. and Stammer, D., Eds., ESA Publication WPP-306

Vapnik VH (1983) Reconstruction of Empirical Laws from Observations (in Russian). Nauka, 447 pp

Vinayachandran PN, Saji NH, Yamagata T (1999) Response of the equatorial Indian Ocean to an unusual wind event during 1994. Geophys Res Lett 26:1613–1616

Walker GT, Bliss EW (1937) World weather VI. Mem Roy Meteor Soc 4:119–139

Weng H, Ashok SK, Behera S, Rao A, Yamagata T (2007) Impacts of recent El Nino Modoki on dry/wet conditions in the Pacific Rim during boreal summer. Clim Dyn. doi:10.1007/s00382-007-0234-0